WindSat On-Orbit Warm Load Calibration

Elizabeth M. Twarog, William E. Purdy, Peter W. Gaiser, *Senior Member, IEEE*, Kwok H. Cheung, and Bernard E. Kelm

Abstract—Postlaunch calibration of the WindSat polarimetric microwave radiometer indicates the presence of thermal gradients across the calibration warm load during some portions of the year. These gradients are caused by reflected solar illumination or eclipse and increase total calibration errors. This paper describes the WindSat warm load and presents the measured on-orbit data which clearly illustrate the anomalous responses seen in the warm load calibration data. Detailed thermal modeling predictions of the WindSat on-orbit performance are presented along with the satellite orbital geometry model with solar inputs in order to explain the physical causes of the thermal gradients. To reduce the resultant calibration errors during periods of anomalous warm load behavior, a correction algorithm was developed which uses the physical temperatures of the gain stages in the receiver electronics to calculate an effective gain. This calibration algorithm is described, and its performance and expected accuracy are examined.

Index Terms—Microwave radiometer, radiometer calibration, remote sensing, WindSat.

I. INTRODUCTION

WINDSAT is a satellite-based multifrequency polarimetric microwave radiometer developed by the Naval Research Laboratory for the U.S. Navy and the National Polar-orbiting Operational Environmental Satellite System (NPOESS) Integrated Program Office (IPO) [1]. It is designed to demonstrate the capability of polarimetric microwave radiometry to measure the ocean surface wind vector (speed and direction) from space. The sensor provides risk reduction for the development of the Conically scanned Microwave Imager Sounder (CMIS), which is planned to provide wind vector data operationally starting in 2010. Launched on January 6, 2003, WindSat is the primary payload on the Department of Defense Coriolis satellite.

The WindSat receivers are total power radiometers operating in discrete bands at 6.8, 10.7, 18.7, 23.8, and 37.0 GHz. The 10.7-, 18.7-, and 37.0-GHz channels are fully polarimetric, while the 6.8- and 23.8-GHz channels are dual polarized only (vertical and horizontal). All receivers are calibrated each scan (every 1.89 s) by using a two-point calibration method based on the heritage design of other spaceborne imaging radiometer systems such as the Special Sensor Microwave/Imager (SSM/I) and the Tropical Rainfall Measuring Mission (TRMM) Microwave Imager (TMI) [2], [3]. Because the WindSat receivers

are highly linear, this two-point calibration technique is sufficient to calibrate the radiometer measurements. In this method, the radiometer feedhorns pass beneath stationary warm and cold targets located above the WindSat deck. The cold calibration point is achieved through a secondary reflector with a constant view of cold space, and a thermally isolated blackbody load provides the warm calibration point. The WindSat warm load construction and location on the structure is typical of other previously flown warm loads and planned CMIS design. In order for the feedhorns to safely pass beneath the warm load, the load must stand off away from the deck surface. Previous experience (SSM/I, TMI) indicated a thermally isolated load, such as the WindSat design, should be sufficiently thermally stable for sensitive radiometric calibration. WindSat postlaunch calibration has shown that this stability assumption is not the case.

The success of this two-point calibration technique depends on accurately knowing the radiometric brightness of the warm and cold targets. For the cold space measurement, we use a constant 2.7 K.[1] Since the warm load is a black body with emissivity of nearly one, the physical temperature is assumed equal to the radiometric temperature. The physical temperature of the warm load is measured by six platinum resistance thermometers (PRTs) embedded in the aluminum base. A calibration problem will arise with this method if the physical temperature of the base is different from the radiometric temperature of the warm load surface where the radiometers view.

During the WindSat postlaunch calibration, we found periods of operation where the temperatures measured by the PRTs do not accurately reflect the physical temperature of the surface of the load due to the presence of large thermal gradients between the load surface and the load base. These PRT temperature measurement errors increase total calibration errors, resulting in incorrectly calculated brightness temperatures and potentially corrupted measurements of wind vector or other environmental data records (EDRs). To reduce these PRT-based calibration errors, we have developed a correction algorithm which uses the physical temperatures of the gain stages in the receiver electronics to identify anomalous periods and calculate an effective gain. In the WindSat data, the magnitude of the brightness temperature difference between anomalous and stable periods in a single orbit can reach 2 K under worst conditions.

It should be emphasized that the thermal gradients introduced into the WindSat warm load are not due to a manufacturing or design flaw within the load, but are a characteristic problem of this type of calibration system configuration. The position of the load above the structure allows for the possibilities of gradients within the load caused by reflected solar illumination and satel-

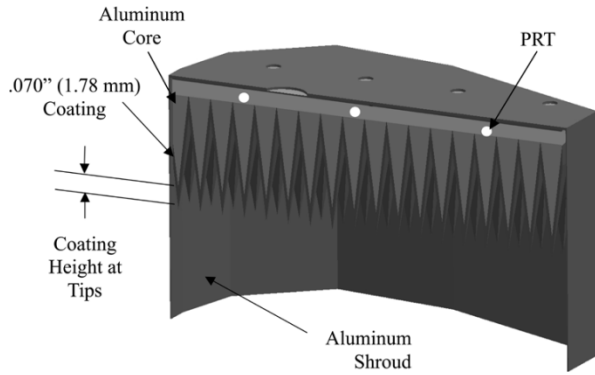[1]http://aether.lbl.gov/www/projects/cobe/COBE_home/cobe_home.html

Fig. 1.   Section view of the warm load showing the aluminum core, the thermal coating of the load, surrounded by the shroud. The position of the deck containing the feedhorns is at the bottom of the figure.

Fig. 2.   WindSat warm load surface with PRT locations (circles) and arcs traced by the feeds noted.

lite eclipse. Presently the calibration data of other spaceborne radiometer systems is being reexamined and early indications are that similar effects also appear in their calibration data. Future systems must take greater care in designing the warm load system to prevent thermal gradients.

This paper describes the WindSat warm load and presents the measured on-orbit data which clearly illustrate the anomalous responses seen in the warm load calibration data. The thermal modeling predictions of the WindSat on-orbit performance are then presented along with the satellite orbital geometry model with solar inputs in order to explain the physical causes of the thermal gradients creating the warm load anomalies. Finally, the WindSat calibration algorithm is described and the performance and expected accuracy of the correction algorithm are examined.

II. Calibration Behavior and Data Characteristics

A. Warm Load Description

The WindSat flight warm load is a well-matched, broadband microwave load composed of tapered pyramids coated with a 70-ml (1.78 mm) layer of Eccosorb CR-117 Epoxy (a microwave absorbing material). It was manufactured and tested by ZAX Millimeter Wave Corporation. Fig. 1 shows a section view of the warm load. The WindSat top deck and feedhorns would be at the bottom of this figure. The emissivity of the load was derived through return loss measurements at 6, 11, and 37 GHz, over an incidence angle range of $0°$ to $20°$. The derived emissivity ranges from a low of 0.999 78 at 6.7 GHz to a maximum of 0.999 99 at 37.5 GHz. The calibration target has a teardrop shape to optimize the number of calibration samples per scan while minimizing scan occlusion. The load is housed in a shroud, which extends three inches beyond the tips to ensure excellent coupling and to shade the load from direct solar illumination, thus minimizing thermal gradients across the load. The warm load is passively heated through exposure to the radiator panels on the top deck of the WindSat canister.

To measure the physical temperature of the warm load, six Rosemount PRTs are encapsulated with conductive epoxy in shallow pockets in the aluminum base. The PRTs, which use four-wire configuration, were calibrated with a measurement uncertainty of $0.027 °C$. Fig. 2 shows the surface of the warm load, the locations of the six PRTs, and the paths that the
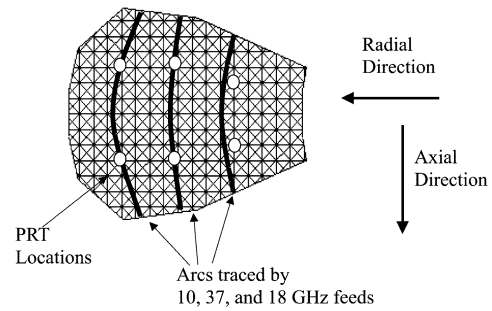
polarimetric feedhorns trace across the load while WindSat is spinning.

The overall WindSat calibration error budget accounts for total calibration errors not to exceed 0.75 K per channel. This means that the combined effect of all calibration error sources, including warm and cold calibration loads, EMI effects, antenna effects, bean efficiency, and receiver nonlinearity, should introduce no more than 0.75-K error on the absolute brightness temperature measurement. The error budget elements for the warm calibration load include emissivity, PRT measurement accuracy, thermal gradients through the load, and thermal stability over measurement time. Emissivity, PRT measurement accuracy (both discussed above), and thermal stability (next section) were easily met. The overall error budget apportioned 0.1 K to thermal gradients through the warm load; this will be discussed in Section III.

B. Two-Point Calibration

The WindSat receivers were designed to be linear ($< 0.1\%$ nonlinearity) over receiver physical temperature ranges from $0 °C$ to $40 °C$. Receiver gain will vary with physical temperature since the behavior of the amplifiers and other components also vary with temperature. The WindSat thermal design maintains thermal stability over one scan so that short-term thermally induced gain variations are not introduced into the gain calculation, and longer term fluctuations (greater than seconds) are calibrated out. The design specified that the temperature of the WindSat canister housing the receivers should not vary greater than $0.005 °C/s$, and this specification is currently being met under operation. At this rate of change, gain stability requirements over one scan are easily met.

We measure the following items from the two calibration points each scan:

- T_{wl}: warm load temperature in Kelvin measured by PRTs in base of warm load;
- T_{cos}: cold space (cosmic) temperature, defined at 2.7 K;
- V_{wl}: warm load counts measured by radiometer; spatial average over a portion of the load;
- V_{cos}: cold space counts, measured by the radiometer.

Using the two calibration points, the gain and offset are calculated as

$$g = (\bar{T}_{wl} - T_{cos})/(\bar{V}_{wl} - \bar{V}_{cos}) \qquad (1)$$

$$T_{off} = T_{cos} - g * \bar{V}_{cos} = \bar{T}_{wl} - g * \bar{V}_{wl} \qquad (2)$$
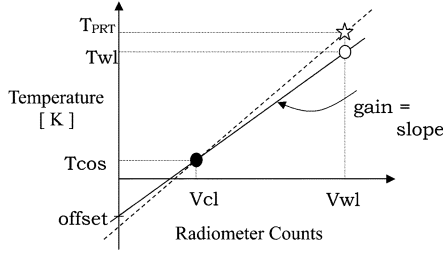
Fig. 3. Two-point calibration illustration. True warm load temperature (open circle) produces true gain and offset (solid line). Erroneous warm load temperature (star) produces incorrect gain and offset (dashed line).

where g is in K/counts and T_{off} is in units of Kelvin. The number of warm load and cold space samples averaged on each scan is different for each frequency band. The warm load temperature T_{wl} is the average of the two PRTs closest to the feed track across the load (see Fig. 2).

Pictorially, this calibration approach is illustrated in Fig. 3 where the open circle represents the true warm load physical temperature and the solid circle represents the cold space temperature. Using these two points, the true gain and offset can be calculated as in the figure (solid line). The fundamental assumption in the calibration warm point is that the PRT temperature represents the radiometric temperature of the warm load. Warm load calibration errors arise when there is a difference between the warm load radiometric average temperature and the temperature reported by the PRTs. If the PRT measurement is not the true temperature of the warm load (star), an erroneous gain and offset are calculated (dashed line). Incorrect representation of the true warm load temperature by the PRT temperature is the source of the WindSat calibration errors which must be reduced.

This calibration is performed once per scan. Then, using the gain and the offset calculated for that scan, and the scene counts V_{scene}, brightness temperatures T_A are calculated for each point in the scene

$$T_A = g * V_{\text{scene}} + T_{\text{off}}. \qquad (3)$$

This approach is only as good as the measurement of the radiometric truth of the warm load, and this is where the WindSat calibration inaccuracies arise.

C. Sun Beta Angle

To understand the calibration issues, the thermal environment created by WindSat's orbit must be examined. This thermal environment is directly tied to the sun angle relative to WindSat's orbit normal, termed beta angle, shown graphically in Fig. 4. Over the course of a year, this beta angle will slowly vary as shown in Fig. 5 from a maximum of $87°$ to a minimum of $57°$. As the beta angle decreases from its maximum, the angle at which the sun's rays strike the spacecraft changes and more solar radiation is reflected into the shroud and reaches the surface of the warm load, as will be discussed in detail in Section III. Beginning in April and lasting into September (beta angles less than about $77°$), this radiation reaching the load surface is strong enough to create significant temperature differences between the warm load surface and the PRTs, with the largest
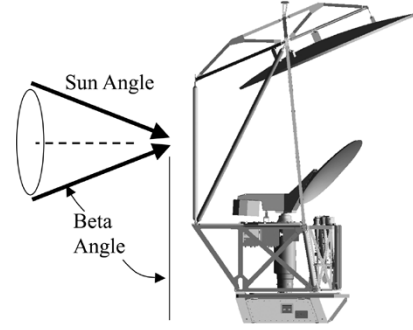

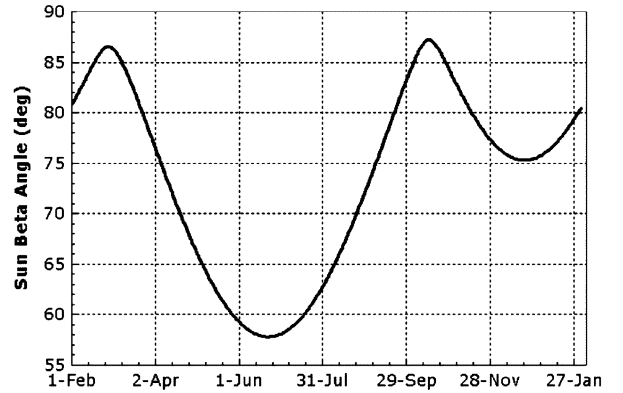Fig. 4. Beta angle definition. Angle between sun and orbital plane.

Fig. 5. WindSat beta angle during 2003. Cycle will repeat for later years of the mission.

temperature gradients at the minimum beta angle. Similar effects are also seen near the winter solstice, as the beta angle approaches $75°$, but the effects are less strong. Also, when the beta angle is less than $63°$, WindSat enters an eclipse season where it is shadowed from the sun by the Earth for periods of up to 17 min per orbit. During these eclipse periods, the abrupt shadowing of the load will cause the nonconducting surface to cool before the base, also creating gradients between the surface and the PRTs. Thermal and orbital details are presented in Section III.

D. Calibration Data Characteristics

The characteristics of the problems introduced by thermal gradients will be illustrated by exploring two datasets from days with different sun beta angles. Note that the data presented in this paper uses only examples of 10.7 and 18.7 vertically polarized data even though the effects of these thermal gradients were evident in all polarizations of all frequency bands. Because the feeds of the different frequency bands view different regions of the warm load, the gradients in one band will have different magnitudes and temporal characteristics from another, but all channels within a band will have similar characteristics. As the beta angle decreases from its maximum, these anomalies appeared first in the 18.7-GHz channels, which see the bottom, or inboard portion of the warm load, followed by the 37-, 23.8-, and 6.8-GHz channels, and then finally by the 10.7-GHz channels, which see the top or outboard portion of the load. Likewise, as the beta angle increases, the problem
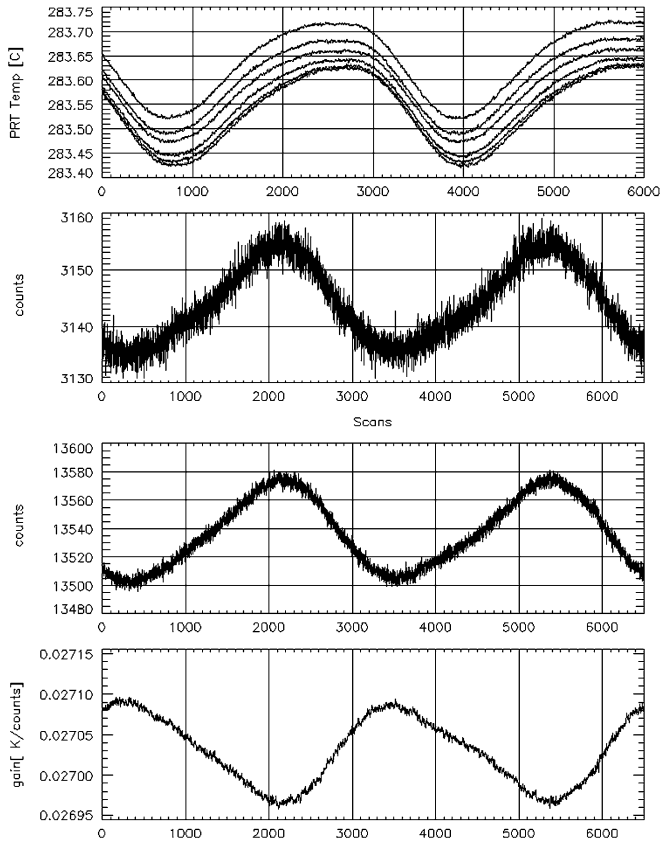
Fig. 6. Measured 18.7 V data from rev 810 (March 4, 2003, Beta 87°) (top) PRT temperatures, (second) cold space counts, (third) warm load counts, and (bottom) calculated gain in K/counts.
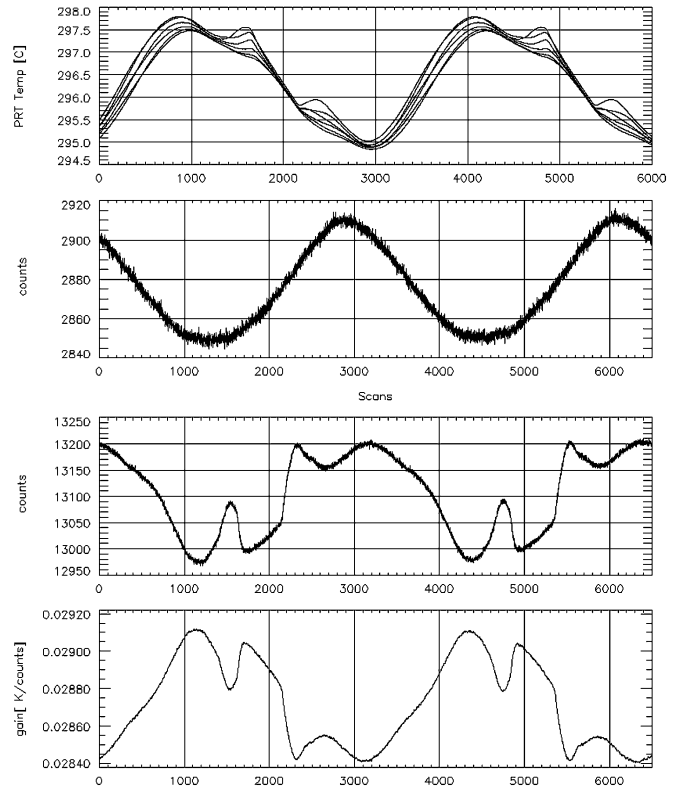

Fig. 7. Measured 18.7 V data from rev 2410 (June 24, 2003, Beta 57°) (top) PRT temperatures, (second) cold space counts, (third) warm load counts, and (bottom) calculated gain in K/counts.

first disappears in the 10.7 channels, followed by the others. The 18.7-GHz examples illustrate the worst case effects of the thermal gradients on the gain calculations and the 10.7-GHz examples illustrate the sensitivity to receiver temperature, as will be discussed in Section VI. Vertical polarization was selected for consistency among the figures, but the characteristics of the anomalies are similar for all the other frequencies and polarizations.

The first dataset is rev 810 from March 4, 2003, with a beta angle of 87°. This set occurs during a period of thermal stability where no load thermal gradients were observed. The second dataset is rev 2410 from June 25, 2003 with a beta angle of 57°. This is from a period of maximum thermal instability where heating and cooling gradients introduce calibration inaccuracies during some periods of each orbit.

Fig. 6 plots two orbits of data from rev 810. Note that there are approximately 3100 scans per 100-min orbit. The top panel plots the six PRT measurements, the middle two panels are the measured cold and warm count measurements, and the bottom panel plots the resulting gain (in K/count), calculated as in (1) and (2). During this rev, all six PRTs exhibit similar behavior. There is an approximately 0.2 K peak-to-peak orbital temperature variation for each PRT, the difference between any two PRTs is less than 0.1 K and the relative difference among all six PRTs remains the same over the two orbits.

Similar sinusoidal orbital behavior is seen in the warm and cold count measurements. Since the cold space target is looking

at a constant view at 2.7 K, the observed variation in counts over the orbit is due to gain variations caused by thermal changes in the receiver and not by scene temperature changes. The sinusoidal orbital behavior in the warm load counts results from a combination of thermal gain changes in the receiver and the measurement of temperature changes in the warm load surface. Under normal calibration, the PRT measurements accurately represent the true load surface temperature and account for these changes in (1) and (2). This PRT and calibration load data results in the gain curve plotted in the bottom panel. This panel illustrates how the gain varies due to thermal changes in the receiver components. Note that gain [K/count] and warm load or cold space measurements [counts], are inversely related, so an increase in gain will result in a lower measurement in counts for a constant scene.

In contrast, the data from rev 2410 shown in Fig. 7 illustrates a more dynamic thermal environment. For the PRTs in the top panel, the peak-to-peak orbital temperature variation is more than an order of magnitude larger than the previous case at closer to 3 K. During the cooling portion of the orbit (e.g., from scans 1000 to 3000), there are two additional secondary peaks (e.g., near scans 1500 and 2400) where the individual PRTs peak at slightly different times. During these peaks, the temperature difference between individual PRTs can be up to 0.5 K. This difference is indicative of the axial gradients across the load (bottom/inboard to top/outboard). In between these two secondary peaks, the PRT measurements indicate that the entire load is cooling to a uniform temperature before the load again begins warming.
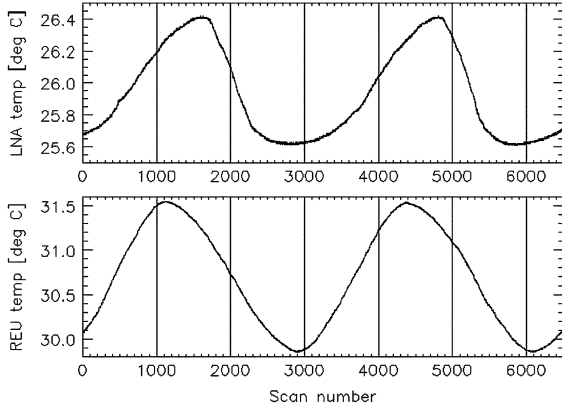
Fig. 8.   (Top) LNA and (bottom) REU temperatures for rev 2410, 18.7 V.

The cold space counts curve in the second panel looks very similar to the curve plotted in Fig. 6. Again, the cold scene is constant, so the orbital variations are indicative of thermally driven gain variations in the receiver electronics. The warm load counts curve exhibits two secondary peaks near the peaks seen in the PRT curve. Recall that though an increase in gain will result in a lower measurement in counts for a constant scene, an increase in scene temperature will result in a higher count measurement. These two secondary peaks result from the warm load increasing in temperature. If the PRTs measuring the physical temperature at the base of the load were accurately measuring the radiometric temperature at the surface of the load, these peaks in both the PRT and warm load measurements would cancel out in (1) and the gain curve would show only the actual slow orbital variation seen in the cold counts. However, artifacts do appear in the gain curve in the bottom panel, indicating that the physical temperature at the base of the load differs from the radiometric temperature at the surface.

To show that the receiver temperatures, and therefore the gain, are stable during this period and that these two secondary peaks are indeed due to temperature gradients through the warm load, Fig. 8 plots the temperatures of the two predetection gain stages [1], the first-stage low-noise amplifier (LNA) and the second stage receiver electronics unit (REU) for rev 2410. Both temperature plots show smooth orbital variations, with no variations near the peaks seen in the PRT or warm load temperatures.

These two datasets illustrate the behavior of the calibration loads under the most thermally stable (no gradients) and the least thermally stable (strong gradients) conditions, indicating that anomalies from the expected warm load behavior are causing gain calculation and calibration errors. The detailed analytical orbital and thermal simulations used to investigate the physical causes of the warm load instability will be discussed in the next section, followed by the development of the gain correction algorithms. These two areas will be tied together with an examination of the correlations between the algorithm and model analyses leading to estimates of the algorithm's accuracy.

III. THERMAL MODEL AND ORBITAL ILLUMINATION ANALYSIS

As indicated in the previous section, differences between the physical temperature measured by the PRTs at the base of the

warm load and the radiometric temperature of the load's surface are indicative of thermal gradients, or heat transfer, through the load. This section gives a qualitative explanation of the heat transfer in the pyramidal structure of the WindSat warm load and then quantitative details about the thermal model used in the analysis of the warm load. Finally, the analysis of the WindSat orbit and the causes of the solar inputs are detailed.

A. Heat Transfer in a Heterogeneous Pyramidal Warm Load Structure

Heat transfer through the warm load is produced by changes to the temperature of the load surface that take a finite amount of time to equilibrate. Since the warm load is not a perfect thermal conductor and since it does have a finite thermal capacitance, it will take a finite period of time to reach a new equilibrium whenever there is a change in its boundary conditions and environmental heat inputs. With a heterogeneous warm load structure, dissimilarity in thermal properties lead to varies transient responses among the constituents and therefore induce a temporal temperature gradient among them. The thermal properties that make the Eccosorb epoxy coating a good material to approximate a blackbody make it a poor thermal conductor. The aluminum core of the load is a better thermal conductor, and heat that passes through the coating can be more quickly equalized through the load than would be possible with an all Eccosorb load. The thickness of the coating is a tradeoff between radiometric requirements (high emissivity) and thermal requirements (quick heat transfer). Fundamental steady-state conductive heat transfer theory relates temperature gradients to the heat flux by the equation

$$Q = kA/L * \Delta T \text{ or } \quad \Delta T = Q/k * L/A \qquad (4)$$

where Q is steady-state heat transfer, k is a conductivity coefficient, A is the cross-sectional area, and L is the length of the conductive path. The restated equation shows that the temperature gradient, ΔT, is proportional to the heat transfer times the ratio of length over area. Coating temperature gradients will be highest between the base and the tips of the warm load pyramids because of the geometric peculiarities at these tips. Pyramid geometry at the tip is such that the coating becomes quite thick (>3 times the thickness of the sides of the pyramid) with a sharp point at the apex as can be seen in Fig. 1. This tall thin pointed area of the coating presents a poor conductive path between the coating extremities and the aluminum core of the load because its ratio of L/A becomes large as the point becomes narrow. It is the thermal isolation of the very tops of the tips that creates the thermal gradients relative to the PRTs embedded in the base that is at the root of the warm load calibration corruption.

The magnitudes of the thermal gradients between the tips and the PRTs can also vary significantly across the face of the load because the illumination reflected onto different areas of the load varies with sun angle. This will be further quantified in the modeling discussion in the next sections. Gradients across the face of the load, where the radiometers do not see a constant temperature as they scan across the load, are less severe than coating-to-PRT gradients as they are minimized in the calibration by averaging a number of samples across the load and also
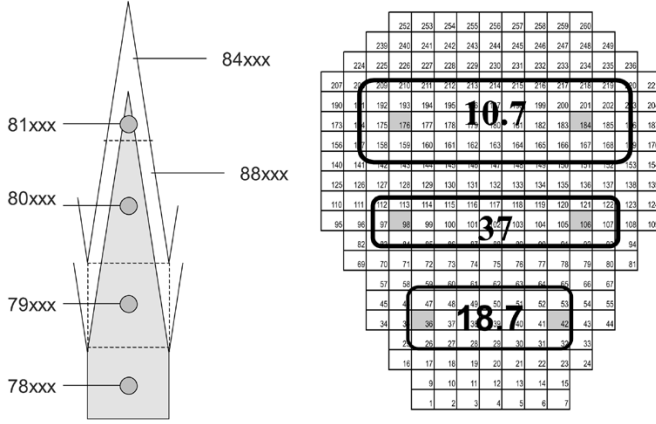
Fig. 9. Nodal schematic of warm load. (left) Single pyramid with sample node numbers indicated and (right) full load with all nodes and calibration zones noted .

Fig. 10. Predicted PRT temperatures at sun beta angle of $57°$.

averaging the measurements from the PRT pair that corresponds to the path of the horn across the load.

B. Thermal Model Analysis

A numerical model was developed to predict the on-orbit temperatures for the warm load design. Prelaunch analysis had predicted gradients between the coating and the base of the load as well as across the load that were all within the error budget. After launch, it became apparent that this was not the case and the gradients were larger than expected. Therefore, we updated the thermal model by adding as-built properties with more sun-angle cases. We analyzed the results of the revised thermal analysis, focusing on the coating-to-PRT gradients to examine more closely how the thermal inputs were creating the calibration problem.

In the model, the WindSat spacecraft and the warm load system were divided into many small finite volumes called nodes. Fig. 9 shows a nodal schematic for the warm load. The model assumes that the mass, temperature, and other thermal physical properties within each node are homogeneous. These nodes are coupled with internal and external heat sources and heat conductors to formulate a thermal network. In the WindSat low Earth orbit environment, conduction and radiation are the dominant modes of heat transport. The energy balance equation of node i in a thermal network that contains n number of nodes can be written as

$$m_i c_i \frac{dT_i}{dt} = \dot{Q}_i + \dot{Q}_{\text{Solar}} + \dot{Q}_{\text{albedo}} + \dot{Q}_{\text{Earth IR}}$$
$$+ \sum_{j=1}^{n} \frac{k A_{ji}}{l_{ji}} (T_j - T_i) + \sum_{j=1}^{n} \sigma \epsilon_j F_{ji} A_j \left(T_j^4 - T_i^4 \right). \quad (5)$$

The left side of the equation represents the rate of change of internal energy of node i, which is the sum of all internal (Q_i) and external $(Q_{\text{Solar}}, Q_{\text{albedo}}, Q_{\text{Earth IR}})$ heat sources that exert on node i, plus the heat energy transferred from the surrounding nodes through both conduction and radiation. The term m is mass and c is thermal capacitance. The external heat sources and the radiation couplings $(\sigma \varepsilon_{ji} F_{ji} A_j)$ were computed with a computer code called the Thermal Synthesizer
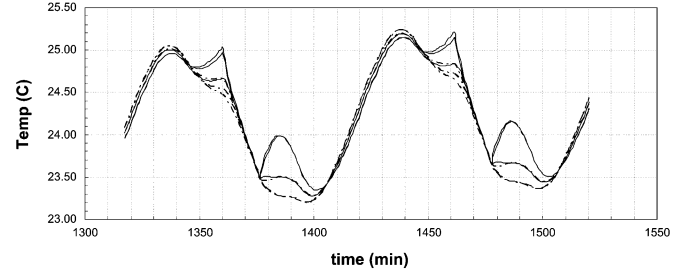
System (TSS),[2] which is based on the principle of the Monte Carlo ray tracing method. Our analysis assumed all radiation surfaces were gray and diffuse. Therefore, the thermal and optical properties of the radiation surfaces are independent of wavelength and direction. Once all the heat sources and thermal couplings were defined, the thermal network was solved by SINDA,[3] which is a numerical analyzer/solver commonly used for spacecraft thermal systems. In our transient analyses, an implicit forward/backward differencing numerical scheme was selected to solve the finite difference equations derived from the thermal network. This numerical scheme averaged the temperature derivatives with the current and the next numerical time steps, and has truncation errors of second order in time and first order in space. This modeling technique is standard practice in satellite design.

Throughout an orbital season, the sun beta angle of WindSat varies from $57°$ to $87°$ as was shown in Fig. 5. Four sun beta angles ($57°$, $63°$, $75°$, and $87°$) were selected for analyses due to their unique thermal environments. At sun beta angles of $63°$ and above, WindSat has full sun illumination for an entire orbit without solar eclipse. Below $63°$, the duration of eclipse slowly increases to a maximum eclipse period of 17 min at the sun beta angle equal to $57°$.

Fig. 10 shows the simulated PRT temperatures of the warm load at sun beta angle of $57°$. This beta angle is comparable to that of rev 2410, the PRT temperatures of which are shown in Fig. 7. The thermal model did reasonably well in predicting the trend of the warm load temperature transients and the temperature gradients at the warm load aluminum base, namely the shapes of the curves with respect to position in time during the orbit. However, the predicted peak-to-peak temperature change is about 2 °C, which is less than the 3 °C measured during rev 2410, showing that the model has underpredicted the magnitudes. The predicted gradients will be further discussed in the algorithm analysis of Section V.

The coating temperature predictions are of particular interest in the WindSat calibration problem. The temperature was predicted throughout the base and coating of each pyramid of the warm load with node locations shown on a sample pyramid on the left side of Fig. 9. The nodes that correspond to the areas of the warm load used for the calibration of particular channels are also highlighted in the figure. Although thermal prediction showed temperature uniformity within 0.4 K throughout a given

[2]Ver. 9.13, Space Design Corp., Houston, TX. http://www.space3d.com.
[3]System Improved Numerical Differencing Analyzer, Version 4.0, SINDA, Cullimore and Ring Technologies, Inc., Littleton, CO. http://www.crtech.com.
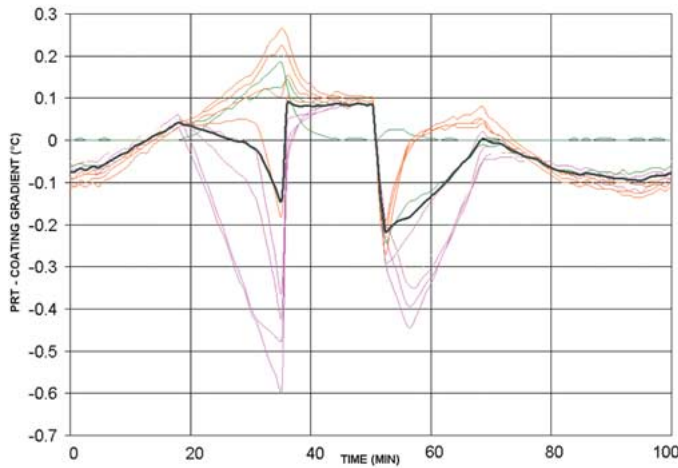
Fig. 11. Modeled temperature gradients predictions between PRT and a subset of tips in the 18.7 calibration zone for rev 2410, Beta 58. Curves are color-coded based on location in calibration zone. Orange lines correspond the top of zone, green to middle of zone, and pink to bottom of zone.

pyramid, it is possible that the radiometers could see a larger temperature gradient across the tip and sides of the pyramid. The relatively coarse nodal division of the pyramid in the thermal model tends to smooth out the gradient effects at the very tip of coating. If the radiometers are more sensitive to the temperature at the very tip of the coating rather than the bulk temperature of the pyramid, the deviation between model prediction and the detected temperature can become significant enough to cause errors in calibration.

Previous modeling of wedge-shaped corrugated microwave absorbers at millimeterwave frequency [4] indicated that the radiometric contribution of the tips to the overall warm load emissivity was less significant at lower frequencies (60 GHz) than at higher frequencies (325 GHz). The author also hypothesized that the tips of a pyramidal structure would have lower overall contribution than wedge tips based on their smaller tip volumes. From this, it was expected that at the much lower WindSat microwave frequencies, the tip contribution to the overall radiometric temperature of the load would be small and the coarse nodal division would be sufficient. More detailed modeling and infrared imaging of other warm loads done after WindSat's launch has shown that a very small portion at the very top of the coating point can have differences approaching 10 K relative to the PRT [5], [6]. While it seems surprising that such small area can contribute such a large effect to the overall calibration, WindSat calibration measurements indicated that that this very localized tip temperature does drive the large gradient effects. Modeling verification of this behavior requires further research.

The most telling uses of the thermal analysis came from calculations of the behavior of the temperature gradient between each tip and the PRT. This gradient is simply a calculation of the difference of each tip temperature and the temperature of the nearest PRT. Fig. 11 has plots of these temperature gradients for a subset (for figure clarity) of pyramids within the calibration zone for 18.7-GHz during two orbits of our most dynamic thermal environment, rev 2410 at Beta 57. The heavy line on the plot which shows the unweighted average gradient between the

PRTs and all of the tip temperatures is expected to be representative of the calibration inaccuracy if the radiometers are in fact highly sensitive to the tip coating temperature.

Looking at each of the tip temperatures relative to the PRT temperature shows large variations in gradient during certain periods in the orbit (i.e., temperature predictions between -0.6 K and 0.25 K at time $= 35$ s in Fig. 11), while in other portions of the orbit the gradients are quite similar to one another and relatively small. This correlates very well with the observations of stable and unstable periods in the flight data, as will be discussed in the next section. It is important to observe that during the unstable periods, some tip temperatures are predicted to be warmer than the PRTs, while other tips within the same calibration zone are predicted to be cooler caused by the uneven heating of the load. The fact that just one calibration zone has both positive and negative gradients highlights the challenge of the warm load calibration anomaly prediction and resolution.

Prelaunch thermal models successfully predicted the existence of axial and lateral gradients between the coating and PRTs, along with the basic shape of the gradient curve over the seasonal and orbital changes, but underpredicted the magnitude of the problem. Recall from Section II-A that 0.1 K was budgeted to gradient effects. The resulting errors in brightness temperature are not within the designed calibration error budget of 0.75 K.

C. Orbital Analysis

During the postlaunch calibration phase, after the magnitude of the warm load calibration problem became apparent, we performed an analysis of the WindSat orbit and the sun position to study what the solar inputs to the warm load were and how they varied both over an orbit and at different times of the year. Using this orbital analysis, we compared the predicted solar input to the WindSat calibration data to explain the timing of the observed anomalies.

This orbital analysis was performed using Analytical Graphic's "Satellite Toolkit (STK)" software.[4] STK is the standard orbit dynamics toolkit of spacecraft engineers, allowing users to perform astrodynamic simulations and see resulting data both analytically and visually. For this analysis, an accurate polygonal model of the full WindSat payload was built. The model included the spinning and stationary portion of the WindSat payload, the calibration loads (including the warm load pyramids inside the shroud), and the main reflector dish with its support structure. A view of this full WindSat model as utilized in our STK analysis is seen in Fig. 12.

To begin this analysis, we first performed simulations propagating WindSat's orbit through times of interest and showing a display of this model flying in orbit with the proper spacecraft attitude. A virtual camera was positioned in a three-dimensional view aimed along the path of incoming solar rays so we could watch a video of the instrument in orbit from the point of view of the sun. This allowed us to qualitatively evaluate what parts of the WindSat payload, particularly at the warm load, were directly receiving solar energy. This also provided excellent intuitive understanding of the changing orbital conditions for the
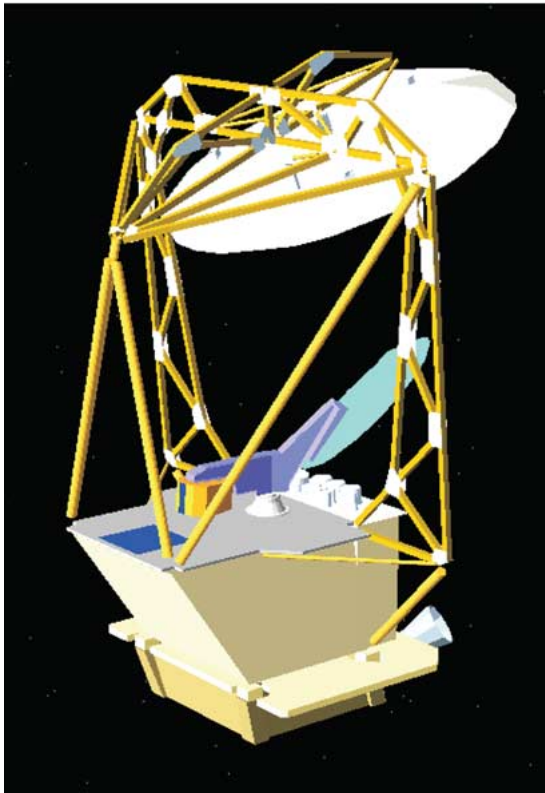
Fig. 12. WindSat model as used in STK analysis.
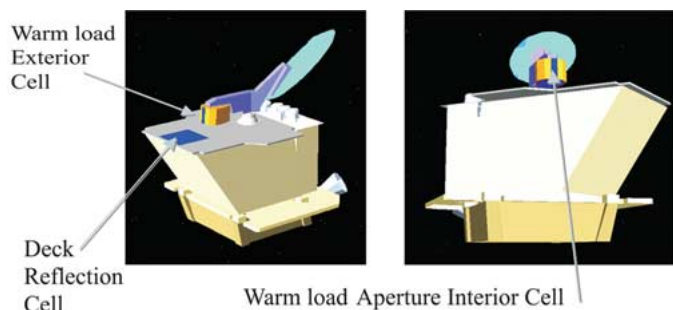

Fig. 13. Pseudo-solar-cell locations.

Fig. 14. Pseudocell output over two orbits.

warm load. By simulating orbits throughout the WindSat mission range of solar beta angles, we were able to conclude that solar energy never directly reached the warm load surface. However, as a function of the beta angle and satellite position in the orbit, there were periods where solar energy reached the interior faces of the warm load shroud, heating these surfaces and potentially reflecting off these surfaces to the load surface, and other periods where the flat spun deck of WindSat could potentially reflect energy into the warm load interior. Additionally, we could see that the main reflector and its support structure were not blocking incoming solar radiation or influencing the warm load heating, so for analysis purposes this structure was then hidden from view, as seen in Fig. 13.

In addition to orbital dynamics analysis, STK has the capability to analyze solar panel power generation on a spacecraft. Solar panel power is a function of orbit geometry, spacecraft and solar panel orientation, self-shadowing of the solar panels by spacecraft geometry, and the resultant area and incidence angle of the solar panel as seen b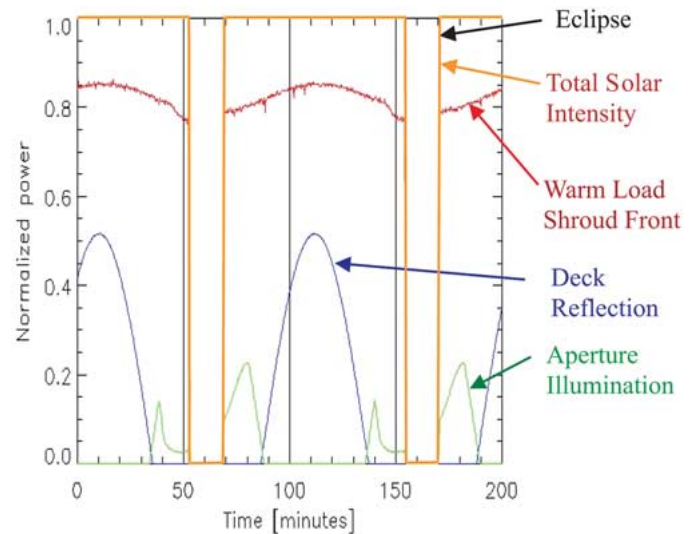y the solar rays. This capability was utilized in our WindSat analysis by creating virtual solar panels in the STK simulation and measuring the power generated by these panels. Such virtual solar panels are referred to as pseudocells as they were not intended to create an actual power measurement, but rather a measure of relative solar energy reaching each of the defined areas. To quantitatively analyze the solar energy reaching the warm load, three pseudocells were created on or around the warm load in the STK simulation.

The pseudocells used in this analysis were positioned across the warm load shroud aperture, on the warm load shroud exterior surface, and on the flat reflective spinning deck of the WindSat payload. Fig. 13 shows the location of these three pseudocells. The cell across the shroud aperture is intended to indicate periods of the orbit when solar energy is directly reaching the interior of the warm load, while the cell on the deck is intended to indicate periods of possible reflection off this deck into the warm load. The cell on the shroud exterior indicates the variation of total incident solar power on the load structure. The calculated power at each of these cells is then normalized by the area of that cell so that the relative magnitudes may be directly compared. Note that the views shown in Fig. 13 are representative of the sun's eye view of the warm load near summer solstice at the height of the thermally unstable season. The left-hand image allows one to visualize sunlight bouncing off the reflective top deck into the warm load shroud during the portion of the orbit where the sun angle comes from above the deck. The right-hand image allows one to see the sunlight's path into the aperture during the portion of the orbit where the sun angle comes from below the deck.

Due to self-shadowing from the rotating deck structure as WindSat spins, the amount of power reaching these pseudocells, particularly the warm load aperture cell, varies as the spun deck completes its 360° rotation every 2 s. To simplify the analysis process, and allow the orbit propagator in the software to have a reasonable step size, an analysis was performed to determine the best representative fixed spin angle. It was determined that a fixed spin angle of 45° provided a power output that well represented the mean results obtained with a spinning deck, and all subsequent analysis was performed with this fixed spin angle.

With these pseudocells built into the STK simulation, several orbit periods representing a range of beta angles were simulated, and measurements of normalized solar intensity at each of these locations were plotted. An example of two orbits of results for a beta angle of 57° (comparable to rev 2410) is shown in Fig. 14. Also plotted is the total solar intensity, which is equal to zero when WindSat is in eclipse. Note that the double-peaked shape of the aperture illumination curve results from the fixed spin angle in the analysis. A spinning WindSat would produce a curve with an envelope similar to the shape of the deck reflection curve. These data were studied along with warm load counts and PRT measurements to find the most thermally stable portions of the orbit for warm load calibration. The correlation of plots of the type shown in Fig. 14 to comparable WindSat flight data provided good understanding of the relationship between warm load illumination and warm load anomalies. Further discussion of the correlations between the orbital analysis, WindSat flight data, and the gain correction algorithm is presented in Section V.

IV. GAIN CORRECTION ALGORITHM

The objective of the following modeling effort was to calculate the receiver gain without relying on PRT measurements during periods of large coating-to-PRT gradients. To do this, the gain correction algorithm must use the available measurements that can be considered truth or a close approximation. The cold and warm load counts are an accurate measurement of the radiometric temperature of cold space and the warm load surface, respectively. These measurements are also influenced by thermally driven changes of receiver gain and offset. The WindSat system monitors temperature telemetry throughout the receiver chains with thermistors on each of the 22 LNAs, each of the 11 REU pairs [vertical/horizontal, $+45/-45$, left and right circular polarization (LCP/RCP)] and each of the five DEUs (by frequency band). These data give us accurate knowledge of temperature variations along each receiver chain. The gain correction algorithm development assumed that the warm load counts, cold space counts, and receiver temperature variations can be trusted at all times, while PRT temperatures are valid only during stable periods of an orbit.

We first designed an algorithm based solely on cold space counts, which are never corrupted by varying solar inputs. This algorithm provided improvement in some channels, but was not able to consistently match the calculated gain accurately during thermally stable orbits. Although eventually rejected, the description of this algorithm is included here for completeness. The second algorithm combines cold space counts with receiver component temperatures. This algorithm properly matched all the signatures observed in the thermally stable data.

Each algorithm uses gain calculated the conventional way [g_{calc}, defined as g from (1)] as a starting tie-point in a stable period of the orbit, where we believe the PRT measurements accurately reflect the radiometric temperature of the load, and then propagates that gain across unstable periods. The tie-point was selected during a thermally stable region in the orbit where the six PRTs consistently track each other closely and show no indication of front-to-back or side-to-side thermal gradients across the face of the load. The selection of the tie-point location
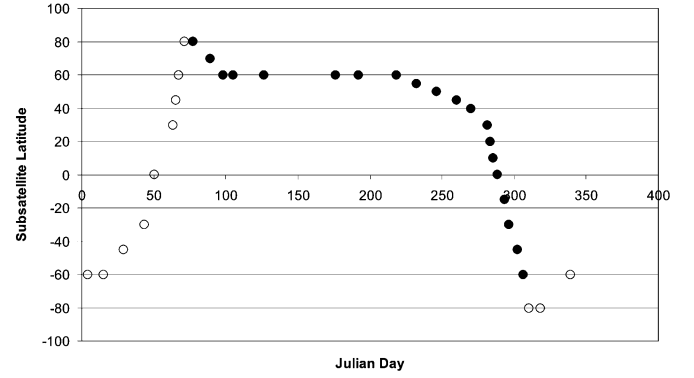

Fig. 15. Plot of subsatellite latitude point for tie-points used in the gain calculation algorithm. Open circles indicate that the tie-point is on an ascending rev, and solid circles indicate a descending rev.

was corroborated with the thermal and orbital analyses. At these points, the PRT measurements accurately represent the true temperature of the coating and therefore the gain and offset calculated conventionally are accurate. After analysis of data over one year, the location of each tie-point was defined in terms of the subsatellite latitude position for simplification of the algorithm calculation. While this region was consistently in approximately the same position on the g_{calc} curve (midway up the increasing slope—see Fig. 7), the location with respect to the satellite orbital position is not fixed, but varies slowly throughout the year. Fig. 15 shows the relationship between subsatellite latitude and the tie-point in the gain curve. The open circles indicate that the latitude on the y axis should be used as a tie-point for a ascending rev, and the solid circles indicate tie-points for an descending rev. For a multiple-orbit file, one tie-point is selected in each orbit and the gain is then propagated across unstable periods.

A. Gain Tied to Cold Space

The cold space scene temperature is a measure of the constant cosmic background radiation, so any variation in cold space counts over an orbit are directly the result of gain or offset changes. Based on this, we hypothesized that the true gain curve should vary in the same manner as the cold space curve. With this, we computed a derived gain g_{cold} by starting with the calculated gain g_{calc} at a tie-point and propagating this gain through the rest of the rev by scaling this average gain by the cold counts (C_{cnts})

$$g_{\mathrm{cold}}(t) = g_o * [C_o/C_{\mathrm{cnts}}(t)] \qquad (6)$$

where g_o is the average gain g_{calc} at the tie-point, and C_o is the average cold space counts for the same region.

During a very thermally stable orbit where the PRTs reflect the true surface temperature and the algorithm gain should match the calculated gain, the results were mixed. For the 18.7 V channel, this method closely predicted the general gain shape variation. However, in the 10.7 V channel for the same rev, g_{cold} does not match the g_{calc} except for regions very close to the tie-points. Comparing the T_{off} offset curve to the errors in g_{cold} showed that these regions where the gain is not closely matched seem to be closely tied to the variations in the T_{off} curve.
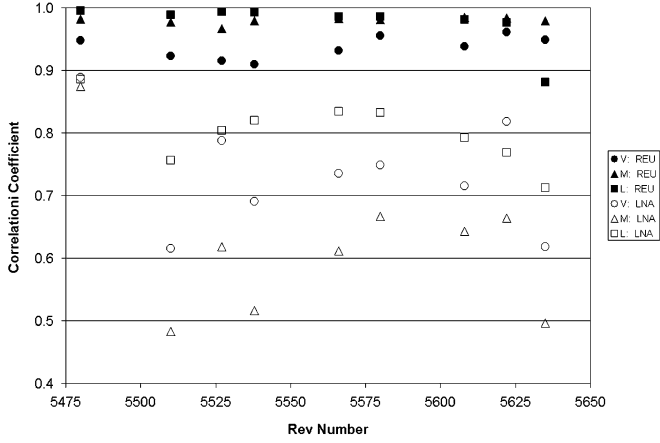
Fig. 16. Correlation between gain and both REU and LNA temperature for 18.7-GHz V, $-45°$, and LCP data in January 2004.

B. Gain Tied to Receiver Temperatures

The next step in the algorithm development examined the correlations between the gain and the available "truth" measurements of the receiver component physical temperatures. We looked at a series of files for the end of January 2004 where the warm load was thermally stable, and examined the correlation between 18.7 gain and the LNA and REU temperatures. For these cases, the gain is very highly correlated with the REU temperature (generally higher than 90%, and higher than 95% for most channels) and less highly correlated to the LNA temperatures (less than 90%). Fig. 16 plots the correlation coefficients between the gain and REU temperatures (solid symbols) and the gain and LNA temperatures (open symbols) for V, $+45°$ (M), and LCP (L) channels. The correlations for the other polarizations are similar. These high levels of correlation between the receiver component temperatures and the gain during thermally stable times allow us to tie the calculated gain behavior directly to these temperatures.

Our main assumption in tying the calculated gain to the receiver temperatures is that the primary source of receiver gain and offset variations is the thermal behavior of the gain stages (REU and LNA) in the receiver chain. This assumption has also been considered in the calibration of other radiometer systems [7], [8]. While there are undoubtedly secondary effects, this is an acceptable starting point before considering other contributing factors. The relationship between receiver gain and receiver physical temperature is independent of any warm load gradients. The WindSat design made for high thermal stability of the receivers (typically $< \pm 1$ C over an orbit) and placed thermistors as close as practical to the amplifiers in the receiver chains. These two design features greatly improve the inherent capability of the correction algorithm.

This correction approach relates the derived gain to the temperature variations of the receiver components. A first attempt assumed that since the majority of the gain in the receiver chain is in the REU, and since the gain and the REU temperature were shown to be highly correlated, the LNA gain temperature effects did not need to be accounted for. This proved untrue. Even though the LNA temperatures are not as highly correlated to the overall gain as the REU temperatures, a significant component
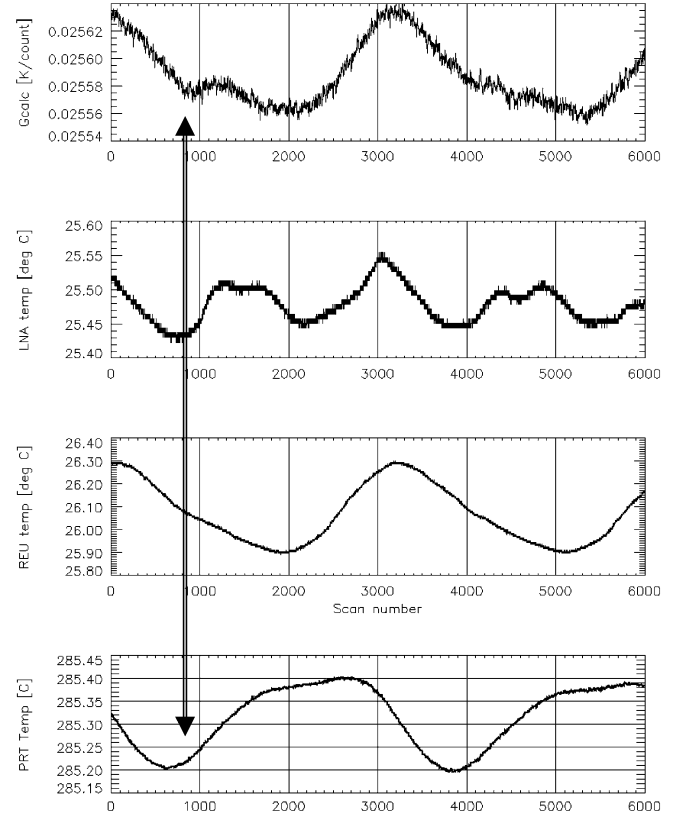

Fig. 17. (Top) g_{calc}, (second panel) LNA , (third panel) REU, and (bottom) PRT temperatures for rev 5826 (February 21, 2004), 10.7 V.

of the gain is contributed by the front-end LNA. During some thermally stable cases there were smaller magnitude variations in the gain curve that the REU thermal behavior alone cannot explain. Since these cases were thermally stable, we believe that these smaller variations are real gain variations and not calibration errors.

Fig. 17 plots the g_{calc} for 10.7 V channel from rev 5826, along with the corresponding LNA, REU and PRT temperatures. The line drawn near scan number 1000 shows that the secondary peaks in the g_{calc} show corresponding peaks in the LNA curve, while no such peaks appear in the REU or PRT temperature curves.

The LNAs and REU of a single receiver chain can vary thermally from one another because they are not physically collocated on a single plate and are able to thermally move independently. In general, the LNAs can react more quickly to changing thermal inputs than the REUs, which have a larger thermal mass. The third gain stage, the digital stage in the DEU, is also a large thermal mass and varies thermally in the same way as the REUs. The DEU temperature is not included explicitly in this correction because it is less highly correlated to the gain than the REU (typically 80%) and its effects would be secondary.

Based on these findings, the receiver temperatures were incorporated into the gain correction using two variable parameters in the following manner. First, a weighted combination temperature vector $T_{\text{RL}}(t)$ was created by adding a fraction of the LNA temperature to the REU temperature

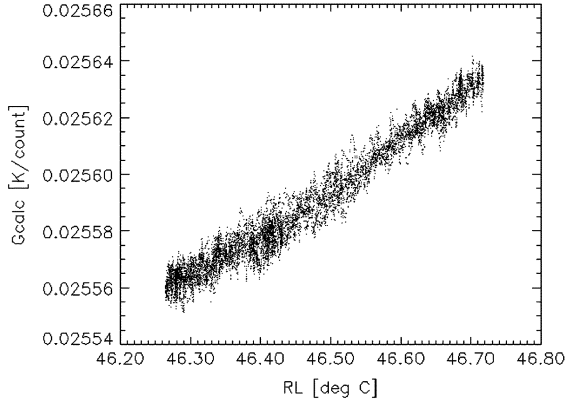$$T_{\text{RL}}(t) = T_{\text{REU}}(t) + FT_{\text{LNA}}(t) \tag{7}$$

Fig. 18. g_{calc} versus combined RL temperature for rev 5800 (February 19, 2004), 10.7 V (Thermally stable case).
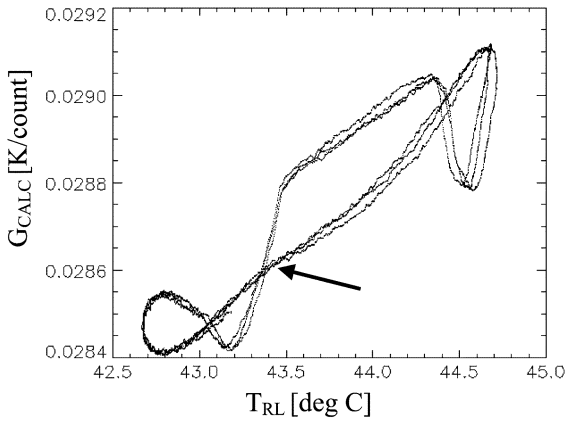

Fig. 19. g_{calc} versus combined RL temperature for rev 2410 (June 25, 2003), 18.7 V (thermally unstable case). Arrow indicates region of linear gain/RL slope that is used in g_{rl} calculation.

where F weights the contribution of the LNA temperature relative to the REU temperature. Based on the WindSat design, it is normally less than or equal to one. This combined temperature vector was smoothed with a running average to take out some of the noise fluctuations. The gain g_{rl} is derived using an average gain g_0 and an average combined temperature T_{RL} calculated at the tie-point. The gain is then propagated using the slope m of the gain versus T_{RL} curve, scaled by a slope scaling parameter S

$$g_{\mathrm{RL}}(t) = g_0 + mS[T_{\mathrm{RL}}(t) - T_{RL,0}]. \qquad (8)$$

It is crucial to calculate the slope m from a linear region in the gain-T_{RL} curve where the gain and the temperature behaviors are highly correlated. The following two figures plot the gain-T_{RL} curves for 10.7 V for a thermally stable case (rev 5800, 2/19/04) in Fig. 18 which can be fit well with a straight line and then for 18.7 V for a thermally unstable case (rev 2410, 6/25/04) in Fig. 19, which obviously cannot be fit with a single line, showing that the tie-point must be chosen carefully. The linear region of that curve near the tie-point where the gain slope is calculated is indicated on the figure. In the calculation of g_{rl}, the slope was determined at one tie-point per orbit, then was linearly interpolated for all the data between tie-points in successive orbits in order to have smooth transitions with no discontinuities from orbit-to-orbit in the final g_{rl} at the tie-points.
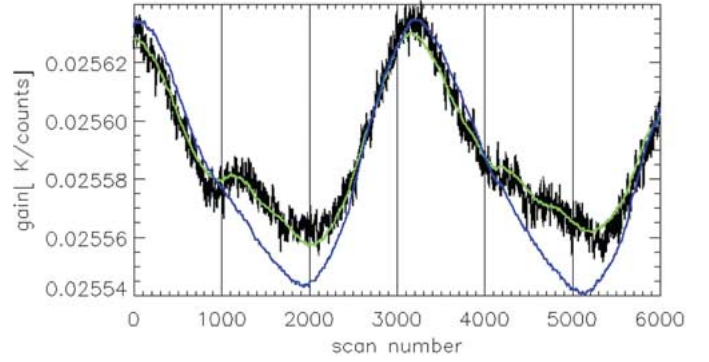

Fig. 20.   (Black) g_{calc}, and g_{rl} [(green) best match, $F = 0.5$, $S = 0.9$; (blue) no LNA contribution, $F = 0$, $S = 1$] for rev 5826 (February 21, 2004), 10.7 V.

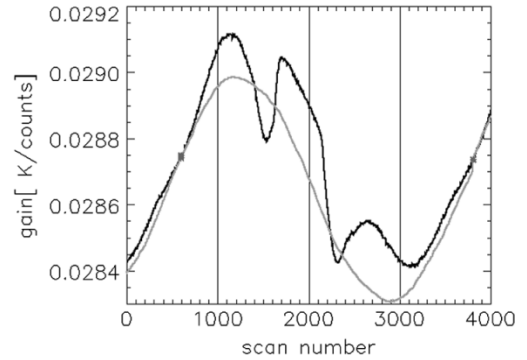Fig. 21.   (Black) g_{calc}, and g_{rl} [(gray) $F = 0.5$, $S = 0.9$] for rev 2410 (June 25, 2003), 18.7 V.

This will also eliminate any calculation error in one orbit from propagating into a following orbit.

The gain g_o was the average of 28 gain samples and the slope m was calculated from 600 points centered on the tie-point position. Fig. 20 plots the results from rev 5826 10.7 V channel with g_{calc} (black) and g_{rl} (green) with $F = 0.5$ and $S = 0.9$. This gain estimation is a good match to the shape of the g_{calc} curve. It matches the overall sinusoidal orbital variation, and also picks up secondary variations (e.g., near scan numbers 1000 and 4700). For comparison, also plotted (blue) is the response of the algorithm if the LNA effects are removed ($F = 0$) to show that the LNA temperature variations must be included to match the secondary variations. This curve with the LNA effects included picks up those secondary peaks that would be missed using the REU temperatures alone. The effects on brightness temperature of the slight gain mismatch between g_{calc} and g_{rl} will be shown in next section.

To determine the fitting parameters, the algorithm was computed for all combinations of S and F in steps of 0.1 from 0.1 to 1.0 for files collected only during thermally stable orbits. The combination of S and F was chosen that had the smallest root mean square difference between the algorithm gain g_{rl} and g_{calc}. This parameter tuning was completed for each polarization and each frequency individually. Once the parameters were selected, the pair would be applied to all revs during the year.

Fig. 21 shows the result of the $g_{\mathrm{rl\ algorithm}}$ for the 18.7 V channel for the thermally unstable case of rev 2410. Again, g_{calc} is plotted in black and g_{rl} is in gray, with the tie-points indicated by asterisks. For this case the REU and LNA temper-

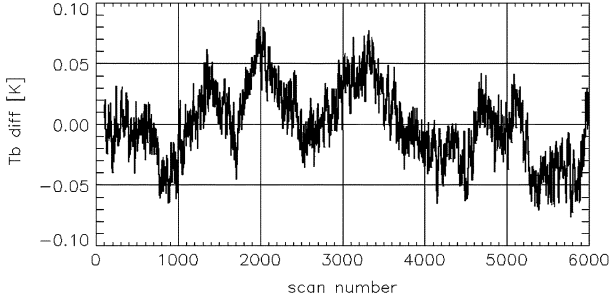Fig. 22. $T_{B,\mathrm{diff}}$ for rev 5826, 10.7 V.

atures all show once-per-orbit sinusoidal variations, and this is reflected in the corrected gain. The result of the differences between g_{calc} and g_{rl} for this case will be examined in the next section.

V. ALGORITHM PERFORMANCE

The algorithm performance is evaluated by comparisons with the PRT-based calibration during periods of maximum thermal stability. Effective hot (~ 300 K) brightness temperatures are calculated for both the original gain and offset ($g_{\mathrm{calc}}, T_{\mathrm{off,calc}}$) and also the algorithm-corrected gain and offset ($g_{\mathrm{rl}}, T_{\mathrm{off,rl}}$) using (3) with a constant V_{scene} of 13 000 counts. The difference between these two brightness temperatures, $T_{B,\mathrm{diff}}$, is defined as

$$T_{B,\mathrm{diff}} = T_{B,\mathrm{calc}} - T_{B,\mathrm{rl}} \qquad (9)$$

and provides a good representation of possible calibration errors for hot scenes. This error is proportional to scene temperature so cooler scenes would have smaller errors. It is important to note that $T_{B,\mathrm{diff}}$ includes both the warm load behavior and algorithm modeling errors and is useful for insight into the warm load behavior.

During thermally stable orbits, $T_{B,\mathrm{diff}}$ provides an estimate of the algorithm modeling accuracy. Where the PRT-based calibration is accurate and we can tune the algorithm to be well matched, we expect the $T_{B,\mathrm{diff}}$ to equal zero. Some small deviation from the correct gain is expected using this first-order model, but as an example of how well the algorithm works during thermally stable times, $T_{B,\mathrm{diff}}$ for the 10.7 V channel of rev 5826 is plotted in Fig. 22. This shows that the maximum brightness temperature difference between $T_{B,\mathrm{calc}}$ and $T_{\mathrm{Br,rl}}$ for this case is <0.1 K. The REU, LNA, and PRT measurements for this rev were shown in Fig. 17. This is a typical value for $T_{B,\mathrm{diff}}$ during stable times. Based on this type of analysis for all WindSat channels, we estimate that the algorithm errors will be on the order of 0.1 to 0.2 K.

In contrast, during the thermally unstable orbits where we know $T_{B,\mathrm{calc}}$ to be corrupted, a nonzero $T_{B,\mathrm{diff}}$ is expected. This difference contains both model errors and the effects of the gradient-affected warm load. We assume that modeling errors are small as in the thermally stable times, but without an additional source of truth to verify that, we must compare the $T_{B,\mathrm{diff}}$ curve to the available flight data items (receiver temperatures, PRT temperatures) and analytical results (orbital analysis, thermal analysis) to determine if there are strong correlations between
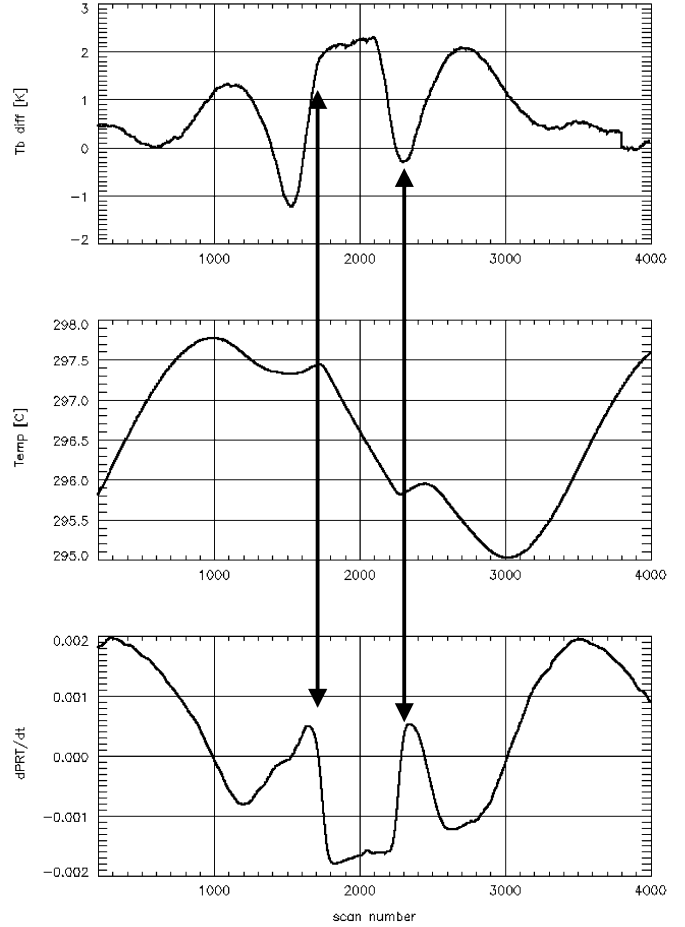

Fig. 23. Comparison of (top) $T_{B,\mathrm{diff}}$, (middle) PRT temperatures, and (bottom) dPRT/dt, for rev 2410, 18.7 V.

these items. Some of these correlations can indicate algorithm inaccuracies while others point to warm load corruption. For example, if $T_{B,\mathrm{diff}}$ had signatures matching LNA temperatures, this would show that the algorithm was not properly modeling the impact of the LNA temperature on the gain. We observed no strong correlations with receiver temperatures, giving us confidence that the model errors during unstable orbits are comparable to the errors predicted during stable orbits.

On the other hand, if $T_{B,\mathrm{diff}}$ had signatures clearly matching analytically predicted coating-to-PRT thermal gradient profiles, this would indicate that the $T_{B,\mathrm{diff}}$ was representative of the magnitude of warm load corruption of the output brightness temperatures. In this case, the magnitude of $T_{B,\mathrm{diff}}$ would be indicative of the brightness temperature errors caused by the warm load anomalies. $T_{B,\mathrm{diff}}$ for one orbit of data from the 18.7 V channel of rev 2410 is shown in Fig. 23, along with the corresponding measurement of an example PRT and its time derivative. Note that the time derivative of the PRT temperature will be positive when the load is warming and negative when the load is cooling. This example shows that for the case of a very warm V_{scene}, the $T_{B,\mathrm{diff}}$ has large deviations from zero during portions of the orbit indicated in the figure, varying between -1 and 2 K. Comparison of the $T_{B,\mathrm{diff}}$ curve with the PRTs and their time derivatives indicated that the large differences correlate with rapid (on the order of several minutes) changes in the PRT
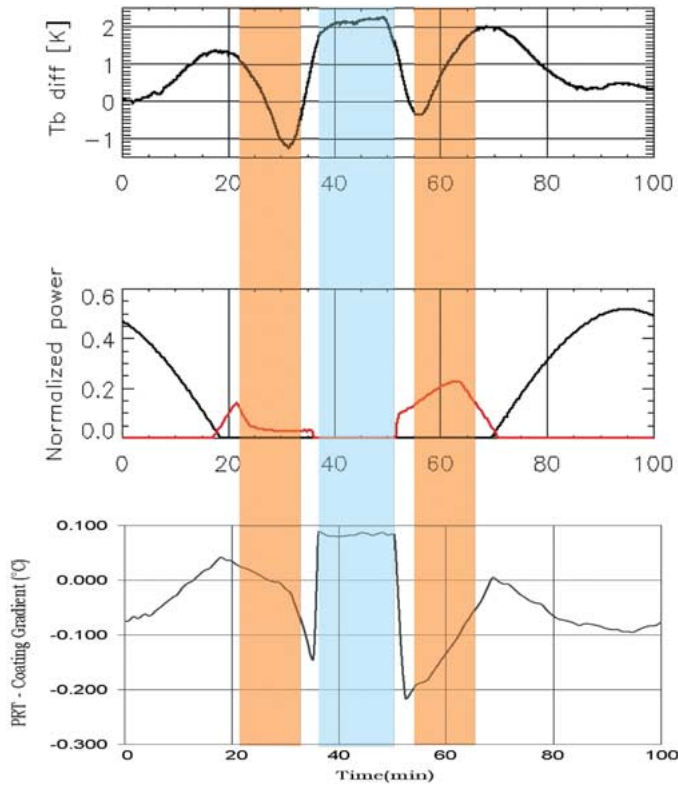
Fig. 24. Comparison of (top) $T_{B,\text{diff}}$, (middle) orbital illumination prediction [(black) deck bounce; (red) aperture illumination], and (bottom) thermal PRT-to-coating gradient prediction for rev 2410, 18.7 V. Blue band indicates eclipse. Orange bands indicate times with large-aperture illumination.

temperatures. The comparison with dPRT/dt shows that as the PRTs warm rapidly, $T_{B,\text{diff}}$ becomes negative, while large positive $T_{B,\text{diff}}$ values correlate with times of rapid cooling. Careful examination of the equations behind $T_{B,\text{diff}}$ shows that $T_{B,\text{diff}}$ will be positive when the coating is cooler than the PRT. So the correlation between a positive $T_{B,\text{diff}}$ and a negative dPRT/dt and vice-versa give confidence that coating-to-PRT gradients are causing the $T_{B,\text{diff}}$ signatures.

The confirmation of the root causes of the gradients comes from comparisons of the same dataset with orbital illumination and with thermal predictions shown in Fig. 24. $T_{B,\text{diff}}$ is shown in the top panel, the normalized power from aperture and deck bounce illumination are shown in the middle panel, and thermal predictions of the average PRT-to-coating gradient are plotted in the bottom panel. Overlaid on the plots are the positions of the orbit corresponding to eclipse (blue shaded band) and periods of maximum aperture illumination (orange shaded bands). The alignment of these signatures shows that aperture illumination is causing the coating to be warmer than the PRTs leading to negative $T_{B,\text{diff}}$ signatures and eclipse is causing the coating to be cooler than the PRTs leading to positive $T_{B,\text{diff}}$ signatures. This causal relationship between the thermal inputs of illumination warming or eclipse cooling gives one confidence that the algorithm is correctly removing the effects of the gradients. Similar signatures were seen on other channels and in many other datasets.

The lack of absolute calibration truth during periods of thermal instability prevents complete validation of the correction algorithm. As shown in Fig. 22, $T_{B,\text{diff}}$ is less than 0.2 K for

orbits with maximum thermal stability, providing indications of the limitations of the algorithm. Maximum $T_{B,\text{diff}}$ values are around 2 K for highly thermally unstable cases such as shown in Fig. 24. The gradient effects we are trying to remove dominate these differences, but algorithm errors contribute to this total. Based on analysis of thermally unstable cases, uncorrected gains will result in brightness temperature errors greater than 1 K approx 9% of the time and errors greater than 0.5 K 21% of the time. Maximum errors will be in the 18.7 channels, which see the portion of the load with the largest temperature variation. The magnitude of these errors can be on the order of ± 2 K at high scene temperatures.

Residual errors in T_B will affect the calculation of EDRs. Sea surface temperature is significantly affected by T_B errors, since that item is dependent on the absolute values of V and H brightness temperatures. Wind direction may not be as strongly affected because the third and fourth Stokes parameters (U and F) are derived by taking the difference between $\pm 45°$ and LCP and RCPs, where similar gradient effects in all channels of a frequency band should cancel. Investigations into the T_B effects on EDR retrievals are currently underway.

VI. CONCLUSION

WindSat was launched in January 2003. During the post-launch calibration phase, anomalous responses were observed between the warm load counts and the measured PRT temperatures during portions of some orbits. The responses deviated from the sinusoidal orbital variation that was observed in the early orbit data, and from what was expected based on the prelaunch thermal vacuum tests performed under controlled thermal conditions. These anomalies produced artifacts in the gain calculation, indicating that the PRTs located in the aluminum base of the warm load were not properly measuring the load surface temperatures observed by the WindSat radiometers.

This paper examines the WindSat warm load thermal behavior in thermally stable and unstable times and describes the causes of the warm load gradients that were observed using orbital and thermal modeling. During the thermally unstable times, there are three external inputs to the calibration load subsystem. Two inputs that result in warming of the warm load are solar radiation reflecting off the rotating deck of WindSat and solar radiation directly into the open shroud aperture. These inputs result in indirect warming of the surface of the load, creating large coating-to-PRT gradients where the coating is warmer than the PRTs. A third input is WindSat entering Earth eclipse for up to 17 min per orbit. At this time, the warm load cools, creating large coating-to-PRT gradients where the coating is cooler than the PRTs. These thermal inputs were confirmed as the source of the calibration anomalies.

The calibration corruption is worst for WindSat in the time periods during and close to eclipse season, with beta angles below 75° and virtually nonexistent for beta angles above 80°. This results in errors greater than 1 K approx 9% of the time and errors greater than 0.5 K 21% of the time. A first-generation algorithm to reduce the errors making use of stable thermal periods and extensive receiver temperature knowledge was developed and tested. The algorithm is capable of correcting the

brightness temperature to within 0.2 K. Algorithm behavior was correlated with thermal behavior and orbital location. Future work will focus on improving and validating this algorithm.

The WindSat warm load configuration is very similar to that used by previous satellite-based microwave radiometers. Data from these systems should be reexamined to confirm that similar warm load errors are not present in the calibration data. In addition, several future microwave radiometers currently in design or development also plan to use a similar configuration. These systems should pay special attention to minimizing thermal inputs to the face of the warm load and should optimize warm load design to minimize coating-to-PRT temperature gradients while maintaining all other performance capability. Creating a post-processing algorithm to completely remove warm load errors is very challenging because once the warm load is corrupted there is a fundamental loss of calibration truth. Calculations of how much these warm load anomalies will affect the environmental data records such as wind vector, sea surface temperature, and atmospheric items are currently ongoing.

REFERENCES

[1] P. W. Gaiser *et al.*, "The WindSat spaceborne polarimetric microwave radiometer: Sensor description and early orbit performance," *IEEE Trans. Geosci. Remote Sensing*, vol. 42, no. 11, pp. 2347–2361, Nov. 2004.
[2] J. P. Hollinger, J. L. Pierce, and G. Poe, "SSM/I instrument evaluation," *IEEE Trans. Geosci. Remote Sensing*, vol. 28, no. 5, pp. 781–790, Sep. 1990.
[3] C. Kummerow, W. Barnes, T. Kozu, J. Shiue, and J. Simpson, "The Tropical Rainfall Measuring Mission (TRMM) sensor package," *J. Atmos. Oceanic Technol.*, vol. 15, pp. 809–817, Jun. 1998.
[4] D. M. Jackson, "Calibration of Millimeter-wave radiometers with application to clear-air remote sensing of the atmosphere," Ph.D. thesis, Georgia Inst. Technol., Atlanta, 1999.
[5] A. McGrath and T. Hewison, "Measuring the accuracy of MARSS—An airborne microwave radiometer," *J. Atmos. Oceanic Technol.*, vol. 18, pp. 2003–2012, Dec. 2001.
[6] M. Plonski, private communication at Plonski Engineering, El Segundo, CA.
[7] K. Al-Ansari, J. M. Riera, A. Benarroch, D. Fernandez, and L. Fernandez, "Calibration procedure of a microwave total-power radiometer," *IEEE Microw. Wireless Compon. Lett.*, vol. 12, no. 3, pp. 93–95, Mar. 2002.
[8] D. A. Thompson, R. L. Rogers, and J. H. Davis, "Temperature compensation of total power radiometers," *IEEE Trans. Microw. Theory Tech.*, vol. 51, no. 10, pp. 2073–2078, Oct. 2003.

Elizabeth M. Twarog received the B.S. degree from the University of Massachusetts, Amherst, and the M.S. and Ph.D. degrees from Northeastern University, Boston, MA, in 1992, 1995, and 1998, respectively, all in electrical engineering.

From 1993 to 1998, she worked as a Graduate Assistant in the Radar Systems Laboratory in the field of polarimetric low-grazing angle radar sea scatter and airborne radar imaging of the coastal ocean. Since joining the Passive Microwave section of the Naval Research Laboratory, Washington, DC, in 1999, she has been involved with microwave spaceborne polarimetric radiometry. She is a member of the WindSat technical and science teams, involved with prelaunch receiver system testing and postlaunch calibration.

William E. Purdy received the B.S. degree in mechanical engineering from the University of Maryland, College Park, in 1986.

He has specialized in spacecraft systems engineering and spacecraft mechanisms over an 18-year career including working at the Naval Research Laboratory from 1986 to 1999. He is currently the proprietor of Purdy Engineering, Poolesville, MD, from 1999 to present. He has performed as a Systems Engineer on the WindSat program with responsibilities for alignments, antenna systems engineering, and mechanical systems engineering. He has worked on 25 spacecraft in a wide variety of roles ranging from subsystem manager to program manager.

Peter W. Gaiser (S'91–M'93–SM'04) received the B.S. degree in electrical engineering from Virginia Polytechnic Institute and State University, Blacksburg, in 1987, and the Ph.D. degree from the University of Massachusetts, Amherst, in 1993, where he studied microwave remote sensing, with emphasis on synthetic aperture interferometric radiometry.

He has been with the Naval Research Laboratory (NRL), Washington, DC, since 1993, and currently Acting Head of the Remote Sensing Physics Branch, Remote Sensing Division at NRL. While at NRL, he has been involved in polarimetric radiometry research. His research interests also include instrument design, data collection, and model development specifically for the purpose of ocean wind vector measurements from space. He is the Principal Investigator for the WindSat spaceborne polarimetric microwave radiometer demonstration project.

Kwok H. Cheung received the Ph.D. degree in mechanical engineering from University of Maryland, College Park, in 1996.

He has over ten years of experience in two-phase thermal/heat transfer systems, including heat pipes, mechanical pumped loops, capillary pumped loops (CPLs/LHPs), and EHD enhanced heat transfer. He is currently a thermal engineer at the Naval Research Laboratory, Washington, DC, where he has worked on several spacecraft programs such as ICM, CAPL3, WindSat, NEMO, and Upperstage. He was the Program Manager for the CAPL3 flight experiment, which was flown successfully on STS-108 to demonstrate a multiple evaporators CPL system in zero gravity.

Bernard E. Kelm received the B.S. degree in aerospace engineering from the University of Maryland, College Park, in 1991.

He is currently an Astrodynamicist in the Spacecraft Engineering Department, Naval Research Laboratory (NRL), Washington, DC. At NRL, he has worked on numerous missions in areas ranging from pure research to mission design and mission operations. He specializes in using high-fidelity computer simulations to aid in astrodynamic analysis.